1 # How symmetry factors cause potential- and facet-dependent
2 # pathway shifts during CO_2 reduction to CH_4 on Cu electrodes

3 Alejandra Rendón-Calle,[a,b,†] Qi Hang Low,[c,†] Samantha Hui Lee Hong[c], Santiago Builes,[a,*]

4 Boon Siang Yeo,[c,*] and Federico Calle-Vallejo[b,*]

5 [a] *Departamento de Ingeniería de Procesos, Universidad EAFIT, Carrera 49 No 7 sur 50, 050022, Medellín,*
6 *Colombia.*

7 [b] *Departament de Ciència de Materials i Química Física & Institut de Química Teòrica i Computacional*
8 *(IQTCUB), Universitat de Barcelona, Martí i Franquès 1, 08028 Barcelona, Spain.*

9 [c] *Department of Chemistry, Faculty of Science, National University of Singapore, 3 Science Drive 3, Singapore*
10 *117543 and the Solar Energy Research Institute of Singapore, SERIS, National University of Singapore*
11 *(NUS), 7 Engineering Drive 1, Building E3A, #06-01, Singapore 117574.*

12 [†] These authors contributed equally to this work
13 [*] Corresponding authors: sbuiles@eafit.edu.co (S.B.); chmyeos@nus.edu.sg (B.S.Y.); f.calle.vallejo@ub.edu
14 (F.C.V.)

15

16 ## Abstract

17 The deactivation of copper electrodes is a serious problem that can affect the scalability and
18 deployment of CO_2 electrolyzers. The effect is generally attributed to the cathodic deposition
19 of Fe and Zn impurities from the electrolyte. Herein, an experimental-theoretical study
20 shows the existence of potential- and facet-dependent pathways for CO_2 reduction to CH_4
21 on Cu. The small-overpotential pathway deactivates the electrodes, while the large-
22 overpotential pathway does not. Theoretical modeling traces the origin of the deactivation
23 to *COH and *CHO, the two *CO hydrogenation products. *COH, which reduces to *C
24 (precursor to coke), is more stable than *CHO around the equilibrium potential, but its
25 symmetry factor is smaller. Hence, the *COH-based coking pathway opens first until the
26 potential is negative enough for the *CHO-based pathway to dominate. This highlights the
27 often-neglected role of symmetry factors in electrocatalysis design and suggests that small
28 increases in *CHO's symmetry factor can mitigate Cu deactivation.

29

30 **Keywords:** *CO_2 electroreduction; copper; competing reaction mechanisms; deactivation;*
31 *symmetry factor.*

32

Introduction

Copper is well known for its singular ability to catalyze the electrochemical reduction of CO_2 (CO_2RR) [1] toward a variety of hydrocarbons and alcohols such as methane, ethylene, ethanol and 1-propanol [2-4]. If renewable energy is used to drive the process, the much-needed carbon-neutral cycle for chemical and fuel synthesis is achievable [5]. However, the implementation of Cu-based electrolyzers for CO_2RR in the industrial scale is hindered by three factors: (i) the large overpotentials required to overcome the energy barriers for product formation, (ii) the poor selectivity of the reaction on Cu, and (iii) the deactivation of the Cu electrodes during long-term operation. Thus far, considerable efforts have been directed to solving (i) and (ii). This has proven challenging [6], as the rational development of more active and selective Cu-based catalysts for the CO_2RR requires a thorough theoretical and experimental understanding of the reaction mechanisms, which are influenced by local pH, mass transfer, and the interplay at the electrical double layer between solvents, electrolytes, and surface structure [7-10].

Addressing (iii) is also critical, because frequent deactivation during operation is a clear obstacle to the scalability and long-term deployment of Cu electrodes for CO_2RR. The highly influential work by Hori and coworkers attributed the deactivation to the deposition of Fe and Zn contaminants from the electrolyte onto the Cu cathode during CO_2 electrolysis [11]. Thus, solutions to mitigate deactivation by contaminants from the electrolyte include the use of ultrapure salts for preparing the electrolytes and cation-exchange resins to scavenge for these trace metal ions [12].

Interestingly, the possibility of the surface being deactivated and poisoned by reaction intermediates, so often observed in the field of gas-phase thermal catalysis [13], has been generally side-stepped. A notable exception was the study by Dewulf and Bard [14], where CO_2 was suggested to reduce to graphite via formate. Equally noteworthy is that Cu surfaces that tend to deactivate are frequently CH_4-selective [15]. On the other hand, oxide-derived copper catalysts, which reduce CO_2 dominantly to ethylene and ethanol, do not deactivate at the same rate [16, 17]. These observations strongly suggest that, apart from deactivation by trace metal contamination, there could be mechanistic pathways that lead to the deactivation of Cu electrodes during CO_2 reduction, and such pathways should operate particularly while producing CH_4.

Different reaction pathways for CO_2 reduction on Cu have been proposed [18] and several reaction intermediates have been identified, for example, *CO [19], $*C_2O_2H$ [20], and acetaldehyde [21, 22], among others [23]. The surface morphology and the applied potential can significantly affect the product distribution of Cu [24-29] and Cu-based electrodes [30-32], and two main pathways have been proposed for CH_4 formation, namely, one that proceeds through a *CHO intermediate and the other through a *COH intermediate. Further hydrogenation of these two intermediates leads to CH_4 formation. We highlight some of these possible routes: (a) *CHO → $*CH_2O$ → $*OCH_3$ → CH_4, (b) *CHO → *CHOH → *CH → $*CH_2$ → $*CH_3$ → CH_4, (c) *COH → *CHOH → $*CH_2OH$ → $*CH_2$ → $*CH_3$ → CH_4, and (d) *COH → *C → *CH → $*CH_2$ → $*CH_3$ → CH_4 [33-38]. Interestingly, route (d) can lead to the formation of coke due to the early C-O bond scission of *COH to form *C.

In this work, we show that two pathways exist during CO_2RR to CH_4 on Cu at different potentials. The small overpotential pathway deactivates the electrodes, whereas the large overpotential pathway does not. Experiments on Cu(111) and Cu(100) reveal that the onset potentials of the two pathways are facet-dependent. A model with input from experiments and theory is devised to analyze the two competing pathways. Based on the symmetry factors [39] and the kinetic barrier heights of *CO hydrogenation to *COH and *CHO, we trace the origin of the deactivation back to the formation of *COH, which then forms *C and deactivates the electrodes via coking. The different symmetry factors for *COH and *CHO production eventually make the latter more favorable at larger overpotentials, thereby avoiding coking. Consequently, the deactivation of Cu electrodes can be alleviated, while observing high activities for CH_4 formation by applying negative enough potentials.

Our results illustrate that the deactivation of Cu catalysts may not be solely due to their contamination by trace metals, as commonly believed, but may also be a consequence of a parasitic *COH-based coking pathway. To be able to produce CH_4 at low overpotentials, it is advisable to stabilize *CHO with respect to *COH and/or increase its symmetry factor.

Methods

Electropolished polycrystalline copper

Each polycrystalline copper disc (Goodfellow, 99.99%, 0.385 cm^2) was polished successively with SiC paper (Grit 1200, Struers), 15- and 3- μm diamond slurries (Diapro, Struers). The disc was then electropolished at 259.7 mA cm^{-2} for 60 s in phosphoric acid (85% w/w in H$_2$O, Sigma Aldrich), with a platinum wire as the counter electrode. After that, the electrode was thoroughly rinsed with deionized water (18.2 MΩ·cm ultrapure water) and used immediately for CO$_2$RR.

Copper single crystals

The surface of each copper single crystal was gently polished with a 0.25 μm diamond slurry (Diapro, Struers). Next, it was electropolished at 2 A cm^{-2} for 1 s (Autolab PGSTAT100) in a solution consisting of 130 mL H$_3$PO$_4$ (85% w/w in H$_2$O, Sigma-Aldrich), 20 mL H$_2$SO$_4$ (96%, VWR) and 60 mL deionized water. After electropolishing, the single-crystal electrode was rinsed with deionized water and 0.1 mM HClO$_4$ (70%, Sigma Aldrich). The final acid rinsing step aids the restoration of the single-crystal surface after exposure to oxygen from environment [40, 41].

Electrochemical reduction of CO$_2$

The polished Cu discs were used as catalysts for CO$_2$RR. Aqueous 0.1 M KHCO$_3$ (99.995%, Meryer) was used as electrolyte. A three-electrode configuration was used. The reference electrode was Ag/AgCl (saturated KCl; Pine) and the counter electrode was graphite. An anion exchange membrane (AMV, AGC Asahi Glass) was used to separate the cathodic and anodic compartments. The gaseous products were analyzed by online gas chromatography (GC) (Agilent, 7890A), while the liquid products were analyzed by headspace-GC (Agilent, 7890B and 7697A) and high-performance liquid chromatography (Agilent, HPLC-1260 Infinity Series). During each electrolysis period of 120 min, twelve aliquots of gas samples were automatically analyzed by GC at intervals of 612 s. To ensure that the reported data correspond to a system under equilibrium conditions (totally purged of residual atmospheric gases), only data from the 3rd GC measurement and onwards were

120   used in the data analysis. Details of our chromatography systems have been described in our

121   previous work [42].

122   A potentiostat (Gamry reference 600) was used for controlling CO_2 electrolysis. The iR

123   drop was compensated using the current interrupt mode. Unless stated otherwise, the

124   potentials in this work are referenced to the RHE scale using Equation 1.

125     $$U_{RHE} = U_{Ag/AgCl} + 0.197 + 0.059 \cdot pH \tag{1}$$

126   Inductively coupled plasma-optical emission spectroscopy (ICP-OES, Perkin-Elmer

127   Avio 500) was used to verify the presence of metal impurities in the electrolyte

128   (0.1 M $KHCO_3$). The detection limit of ICP-OES is about 0.003 ppm, with a quantification

129   limit of 0.01 ppm.

130   **Characterization of catalysts**

131   X-ray photoelectron spectroscopy (XPS) (Thermo ESCALab 250i-XL, Al Kα radiation)

132   was used to analyze the surface composition of the Cu electrodes. Calibrations of the binding

133   energies were based on the adventitious C_{1s} peak at 285.0 eV.

134   Cyclic voltammetry (CV) was used to characterize the surface structure of the Cu single

135   crystals. The electrolyte used was 0.1 M KOH (99.99%, Meryer) purged with N_2. The scan

136   rate of the CV was 50 mV s^{-1}.

137   Raman spectroscopy was employed to analyze the Cu surfaces. A Raman microscope

138   (Horiba Jobin Yvon) equipped with a He-Ne laser (CVI Melles Griot) of 633 nm wavelength

139   was used. The focusing and collecting of the incident and scattered laser light were carried

140   out using an air objective (Olympus MPlan N, 50×, numerical aperture of 0.75). The

141   backscattered light was filtered by a 633 nm edge filter before being directed into a

142   spectrograph (iHR 320)/ charge-coupled device detector (Synapse CCD). The acquisition

143   time for each spectrum was 60 s.

144   **Computational details**

145   The DFT calculations were performed using VASP [43], the PBE exchange-correlation

146   functional [44], and the PAW method [45]. We used a plane-wave cutoff of 450 eV and the

147   conjugate gradient algorithm for the geometry optimizations. The maximum force allowed

148   for such optimizations was 0.05 eV $Å^{-1}$. To smear the Fermi level, the Methfessel-Paxton

149   method [46] was used with an electronic temperature of 0.2 eV and all energies were

150   extrapolated to 0 K. We used periodic slabs with at least 15 Å of vacuum, and dipole

151   corrections were applied. We simulated slabs with 4 layers, with the bottommost two fixed

152   at the optimized bulk distances for PBE, and the uppermost two and the adsorbates fully

153   relaxed (see Figure S1 in the Supporting Information, SI). Details on the assessment of

154   adsorption free energies for *CO, *CHO and *COH are provided in Section S1 of the SI.

155   The solvation contributions to the adsorption energies were taken from previous works [37],

156   see further details in section S1.2 in the SI.

157   The symmetry factor (β_i), used for single-electron transfer steps in an electrochemical

158   reaction, is defined as the fraction of the electrostatic potential energy affecting the reaction

159   rate [39]. For *CO hydrogenation, β_i is the fractional electron charge transferred to the

160   transition state (TS_i, where i = *COH, *CHO):

161    $$*CO + \beta_i e^- \rightarrow *TS_i \tag{2}$$

162   In this order of ideas, the potential-dependent Gibbs energy required to reach the

163   transition state as ($\Delta G^{\#}_{CO \rightarrow TS_i}$) is given by a constant value calculated at 0 V vs RHE

164   ($\Delta G_{TS_i} - \Delta G_{CO}$) and a correction ($\beta_i \cdot eU$, where e is the elementary charge of an electron)

165   that accounts for the contribution to the Gibbs energy of the applied potential (U):

166    $$\Delta G^{\#}_{CO \rightarrow TS_i} = \Delta G_{TS_i} - \Delta G_{CO} + \beta_i \cdot eU \tag{3}$$

167   Mechanistically, *CO and i = *CHO, *COH differ by one proton-electron pair, so that

168   the reaction free energies for $*CO + H^+ + e^- \rightarrow *i$ are $\Delta G_{CO \rightarrow i} = \Delta G_i - \Delta G_{CO} + eU$ in the

169   RHE scale.

170   **Results**

171   **Experimental CO₂RR on polycrystalline and single-crystal Cu surfaces**

172   The chronoamperometric behavior of the CO₂RR in aqueous 0.1 M KHCO₃ electrolyte

173   over a two-hour period for polycrystalline Cu (denoted as Cu$_{poly}$), Cu(111) and Cu(100)

174   electrodes at -0.90, -1.05 and -1.20 V vs RHE is presented in Figure 1 (see also Figures S2-

175   S3 and Tables S4-S12 in Section S2 of the SI). These three potentials were chosen to

exemplify important catalytic scenarios: significant deactivation, little, and unnoticeable deactivation. Time-dependent production of gaseous products, including CH_4, C_2H_4, CO and H_2, were measured during the CO_2RR.

The production of CH_4 is closely linked to catalyst deactivation due to coke formation [16, 47]. Hence, in this work, we use the geometric partial current density of CH_4 (j_{CH4}) to assess the activity of the catalyst: a decrease in j_{CH4} corresponds to catalytic deactivation. Note, though, that the trends in j_{CH4} are similar to those in j_{CO2RR} (Figure S2). Catalyst deactivation is assessed via the percentage change in the j_{CH4} from the 3rd and 12th GC measurements taken during CO_2RR. The results presented are an average of three sets of measurements.

For Cu_{poly} at -0.90 V vs RHE, CO_2 reduces to CH_4 with activities from -0.01 to -0.03 mA cm^{-2} (Figure 1a; Tables S4-S6). The small j_{CH4} is consistent with previous CO_2RR works on polycrystalline Cu in the same electrolyte [4]. Nonetheless, despite the low formation of CH_4, catalyst deactivation was observed. At -1.05 V vs RHE, more CH_4 was produced, in line with the application of a larger overpotential to drive the CO_2RR. We observed clear and significant deactivation of CH_4 production over the two-hour electrolysis period: specifically, j_{CH4} decreased by 66% from -2.3 to -0.8 mA cm^{-2}. Interestingly at an even more negative potential of -1.20 V vs RHE, deactivation was not observed for CH_4, as shown by its nearly constant production at about -11.1 mA cm^{-2}. However, hydrogen production decreased from -9.9 to -2.4 mA cm^{-2} over the reaction timeframe (Figure S3c; Table S6). This indicates that CO_2RR becomes more facile than hydrogen evolution at this potential during electrolysis. Such a result is distinctive of this work, as previous works showed that H_2 production tends to increase during prolonged reduction reaction, due to contamination by the deposition of unwanted trace metals such as Zn and Fe on the working electrode [11, 12]. Our results at -1.20 V vs RHE indirectly rule out the presence of this effect.
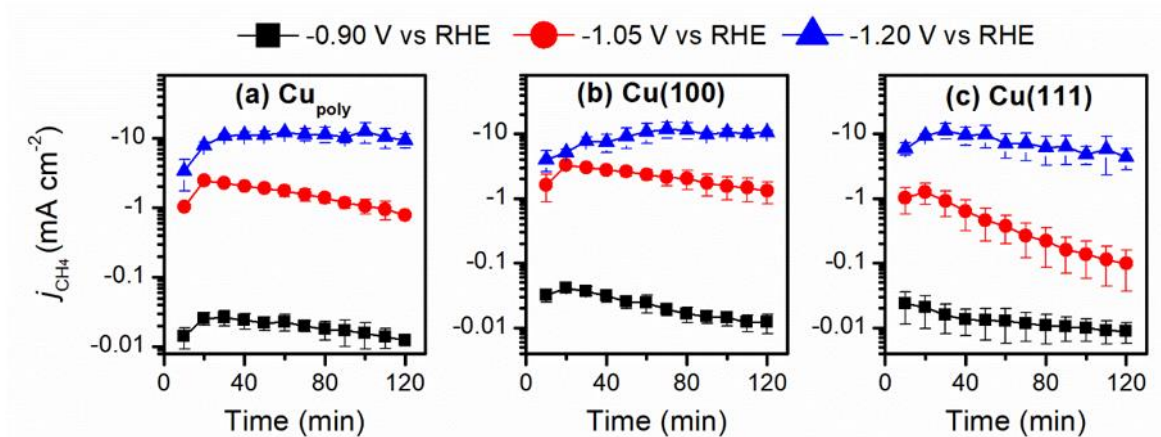
Figure 1. Methane production, as measured by j_{CH4} (mA cm^{-2}), during two-hour CO_2 electrolysis on (a) Cu$_{poly}$, (b) Cu(100), and (c) Cu(111) electrodes at -0.90, -1.05 and -1.20 V vs RHE.

CO$_2$RR was performed on Cu(100) and Cu(111) to determine if the deactivation phenomenon observed on Cu$_{poly}$ is facet-dependent (Figure 1b-c). At -0.90 V vs. RHE, deactivation was observed on Cu(100), where j_{CH4} decreased by 67% from -0.037 to -0.012 mA cm^{-2} (Figure 1b, Tables S7-S9). However, at -1.05 V vs RHE, the same facet showed a smaller deactivation (j_{CH4} decreased by 57% from -3.0 to -1.3 mA cm^{-2}). It is striking that though the activity for CH$_4$ increased due to the larger applied overpotential, its degree of deactivation did not worsen as compared to CH$_4$ production at -0.90 V vs RHE. This suggests that an alternative, non-deactivating pathway for CH$_4$ production could have begun to occur at this potential. Finally, at -1.20 V vs RHE, CH$_4$ production was maintained at about -10 mA cm^{-2}, which was similar to that observed on Cu$_{poly}$.

For Cu(111) (Figure 1c, and Tables S10-S12), minimal formation of CH$_4$ and hence negligible deactivation was observed at -0.90 V vs RHE. At -1.05 V vs RHE, more CH$_4$ production was observed, but with significant deactivation over time: j_{CH4} decreased by 89% from -0.92 to -0.10 mA cm^{-2}. At -1.20 V vs RHE, the deactivation was reduced as indicated by only a 62% change in j_{CH4} from -11.3 to -4.4 mA cm^{-2}. This observation corresponds to the phenomenon observed on Cu(100) at -1.05 V vs RHE and shows that the onset of an alternative and more stable pathway for CH$_4$ evolution occurs on Cu(111) at -1.20 V vs RHE.

Assessing the state of the catalysts after CO$_2$RR

226 The activity of a working catalyst can be altered due to the presence of impurities on its
227 surface or by surface restructuring [11, 48]. Previous reports indicate that Fe and Zn
228 impurities from the electrolyte salts can electrodeposit and deactivate the Cu electrode
229 during CO_2RR [11]. Herein, our analysis of the electrolyte using ICP-OES did not reveal the
230 presence of metal contaminants. XPS was also used to detect metal impurities on a
231 representative Cu_{poly} surface after it was used for CO_2RR at -0.90, -1.05 and -1.20 V vs RHE.
232 The binding energy regions used for qualitative analyses of Zn, Ni and Fe are at 1010-1050
233 (Zn_{2p}), 840-880 (Ni_{2p}) and 40-70 (Fe_{3p}) eV, respectively. No signals were observed in these
234 regions (Figure 2a-c), which suggests that no metal impurities were deposited on the Cu_{poly}
235 surface during electrolysis.
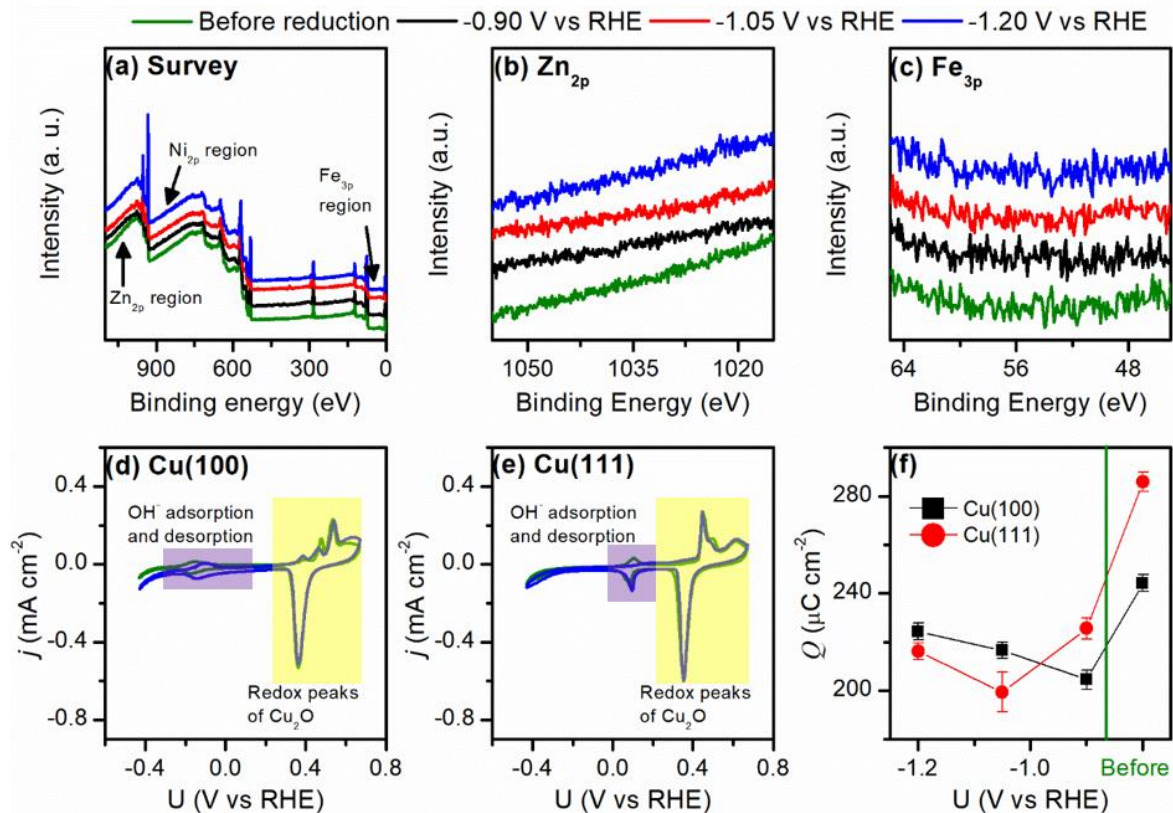
Figure 2. Surface characterization of Cu_{poly}, Cu(100) and Cu(111) before and after CO_2RR. (a) XPS survey
spectrum and high-resolution XPS scan spectra over (b) Zn_{2p} and (c) Fe_{3p} of Cu_{poly} before and after CO_2RR at
-0.90, -1.05 and -1.20 V vs RHE. The regions for common metal impurities in the electrolyte are labelled in
the survey spectra. The data shows that no metal impurities were present on the catalyst surface before and
after CO_2RR. (d) and (e): Representative cyclic voltammograms of Cu(100) and Cu(111) before and after
CO_2RR reduction at -1.20 V vs RHE. Green curve: before reduction. Blue curve: after reduction
at -1.20 V vs RHE. The peaks in the purple shaded region are due to OH^- adsorption/desorption, while the
peaks in the yellow shaded region are from the redox of Cu_2O. No additional peaks were observed, confirming
the absence of metal impurities during CO_2RR. (f) $Q_{Cu(100)}$ and $Q_{Cu(111)}$ obtained for Cu(100) and Cu(111) before
and after reduction at -0.90, -1.05 and -1.20 V vs RHE.

9

248   We are aware that the surface crystallography of the Cu single crystal could change
249   during CO_2RR. Cyclic voltammetry (CV) was then employed to monitor the surface of the
250   catalyst (Figure 2d, e). The similar voltammogram profiles of Cu single crystals before and
251   after they were used for CO_2RR indicate that their surface orientation was largely unchanged
252   during the electrolysis. This finding is also supported by the work of Soriaga and coworkers
253   [49], who showed that both Cu(100) and Cu(111) are stable for at least 4 h when held at -0.9
254   V vs SHE in 0.1 M KOH.

255   OH^- adsorption/desorption peaks were observed between -0.3 to 0 V vs RHE for Cu(100)
256   and between 0 to 0.2 V vs RHE for Cu(111). Peaks from 0.30 to 0.45 V vs RHE belong to
257   copper oxidation/reduction [41, 50]. No other peaks were observed, which further indicate
258   that there were no metal contaminants deposited on the catalyst surfaces after CO_2RR. The
259   areas under the CV oxidation peaks for the monolayer formation of Cu_2O were integrated,
260   according to the method by Fletcher [51]. The charge densities (Q) are indicative of the
261   exposed surface areas of the electrodes (see Section S3 in the SI). The $Q_{Cu(100)}$ and $Q_{Cu(111)}$,
262   of our pristine Cu(100) and Cu(111) surfaces were respectively 244.2 and 285.6 $\mu C\ cm^{-2}$
263   (see Figure 2f). These results agree well with those previously calculated [52], namely 245
264   and 283 $\mu C\ cm^{-2}$ for Cu(100) and Cu(111), respectively.

265   After the Cu(100) and Cu(111) electrodes were used for CO_2RR, we found that the
266   charge densities of the copper oxidation peaks decreased (Figure 2f). This observation allows
267   us to rule out the possibility that the change in CH_4 signals was due to roughening of the
268   catalyst surface during CO_2RR, as it would lead to an increase in $Q_{Cu(100)}$ and $Q_{Cu(111)}$.
269   Instead, we believe that the catalyst surfaces suffered from various degrees of coking during
270   reduction at various potentials, which decreased their exposed surface areas. This is
271   highlighted by the good match of the increase in charge densities on Cu(100) and Cu(111)
272   with the observed onset potentials (-1.05 and -1.20 V vs RHE, respectively) for the
273   alternative non-coking pathway. For example, an increase in the charge density for Cu(100)
274   at -1.05 V vs RHE is observed when compared to that at -0.90 V vs RHE. This could be
275   ascribed to decreased coke formation resulting from the opening of a non-coking pathway
276   for CH_4 production at -1.05 V vs RHE. A similar effect was observed for Cu(111), which
277   occurred only at -1.20 V vs RHE. We further note that the charge densities of Cu(100) and
278   Cu(111) after they were used for CO_2RR at -1.2 V vs RHE were still lower than those of the
279   pristine surfaces. This suggests that the deactivating pathway could operate alongside the
280   non-deactivating pathway, even at high overpotentials.

Carbon species formed during CO$_2$RR could deactivate the Cu catalyst. Thus, we used Raman spectroscopy to characterize the surfaces of the Cu$_{poly}$ electrodes after they were used for CO$_2$ electrolysis at -1.05 and -1.20 V vs RHE (Section S4 in the SI). We did not observe any peaks related to carbide (expected for Cu-*C at ~530 cm^{-1}) [53], and/or amorphous carbon (peaks at 1350 and 1590 cm^{-1}) [54] after 2 h of electrolysis. However, after 4 h of electrolysis, we detected peaks at around 1340 and 1590 cm^{-1}, which are distinctive of the presence of amorphous carbon. Their signal intensities were also notably higher after electrolysis at -1.05 V vs RHE as compared to -1.20 V vs RHE. Based on these results, we propose that during the first 2 h of electrolysis, discrete *C adsorbates could have been formed on Cu, but their weak Cu-*C peaks could not be detected by Raman spectroscopy. After 4 h of CO$_2$RR, more *C moieties are likely to be formed, and these could have aggregated to form amorphous carbon, which has stronger Raman scattering. It is notable that the larger amount of amorphous carbon observed on Cu$_{poly}$ after electrolysis at -1.05 V, as compared to -1.20 V vs RHE, is in excellent agreement with its faster deactivation at the smaller applied overpotential (Figure 1a). The observation of amorphous carbon after prolonged electrolysis is consistent with previous studies [15, 55], where *C/ amorphous carbon was identified as the species that causes catalytic deactivation on Cu surface during CO$_2$RR.

To recap, the characterization of the catalysts before and after CO$_2$RR in Figure 2 indicates that the deactivation of Cu electrodes observed in Figure 1 did not result from changes in surface crystallography or the presence of metal contaminants on the catalyst surface. Instead, deactivation may be a consequence of coking by the generation of reaction intermediates during CO$_2$ electrolysis. The deactivation of the Cu surfaces during CO$_2$RR is also potential- and facet-dependent: the onset potential for constant CH$_4$ production is less negative on Cu(100) (-1.05 V vs RHE) compared to Cu(111) (-1.20 V vs RHE). Since changes in surface structure and poisoning by trace metals can be ruled out as the causes of this phenomenon, the evidence hints toward mechanistic formation of *C/amorphous carbon as a byproduct during the catalytic cycles of CO$_2$RR. Given that the deactivation is potential-dependent, we postulate that there is a "coking" pathway dominating at low applied overpotential. In contrast, at high applied overpotential, there appears to be a non-coking pathway, where *C (common cause for coking) is not formed during CH$_4$ production. In the next section we will combine computational and experimental data to rationalize the experimental observations in Figures 1 and 2.

Theoretical analysis of the CO₂RR

314

315   Herein, by combining DFT-calculated and experimental data, we will argue that CH_4

316   evolution on Cu likely proceeds via two different pathways as the potential is varied. The

317   two pathways diverge from *CO hydrogenation, as *COH or *CHO can be formed. At less

318   negative potentials, CH_4 production proceeds through a mechanism that deactivates the

319   electrode. At more negative potentials, an additional mechanism for CH_4 evolution, that does

320   not poison the electrode, is opened. Importantly, the analysis proceeds by reconsidering the

321   usual experimental approximation that the symmetry factors of electrochemical steps (β) are

322   identical and equal to ½ [39].

323   On the basis of computational analyses, several reaction mechanisms for CO₂RR to CH_4

324   on Cu have been proposed [7, 8, 33-35, 37, 38]. While these mechanisms differ in several

325   aspects, they show that hydrogenation of adsorbed CO (denoted *CO) is the potential-

326   limiting step. There are two possible products of *CO hydrogenation, namely *CHO and

327   *COH. A CO₂RR pathway to CH_4 proceeding via *COH will eventually form *C and/or

328   *CH, both of which might polymerize to coke the electrode. We suggest that *C, rather than

329   *CH, is the coking species, as the formation of acetylene is not typically reported on Cu

330   during CO₂RR [4, 8, 9]. On the other hand, a CO₂RR pathway via *CHO will likely form

331   *CHOH [8, 36], which avoids the formation of *C. These reaction pathways are shown in

332   Figure 3. Note that the steps along the reaction network are electrochemical, as the barriers

333   of chemical steps for C-O bond scissions are considerably larger than the corresponding

334   electrochemical barriers (see a detailed comparison in Table S1) [36, 56, 57].
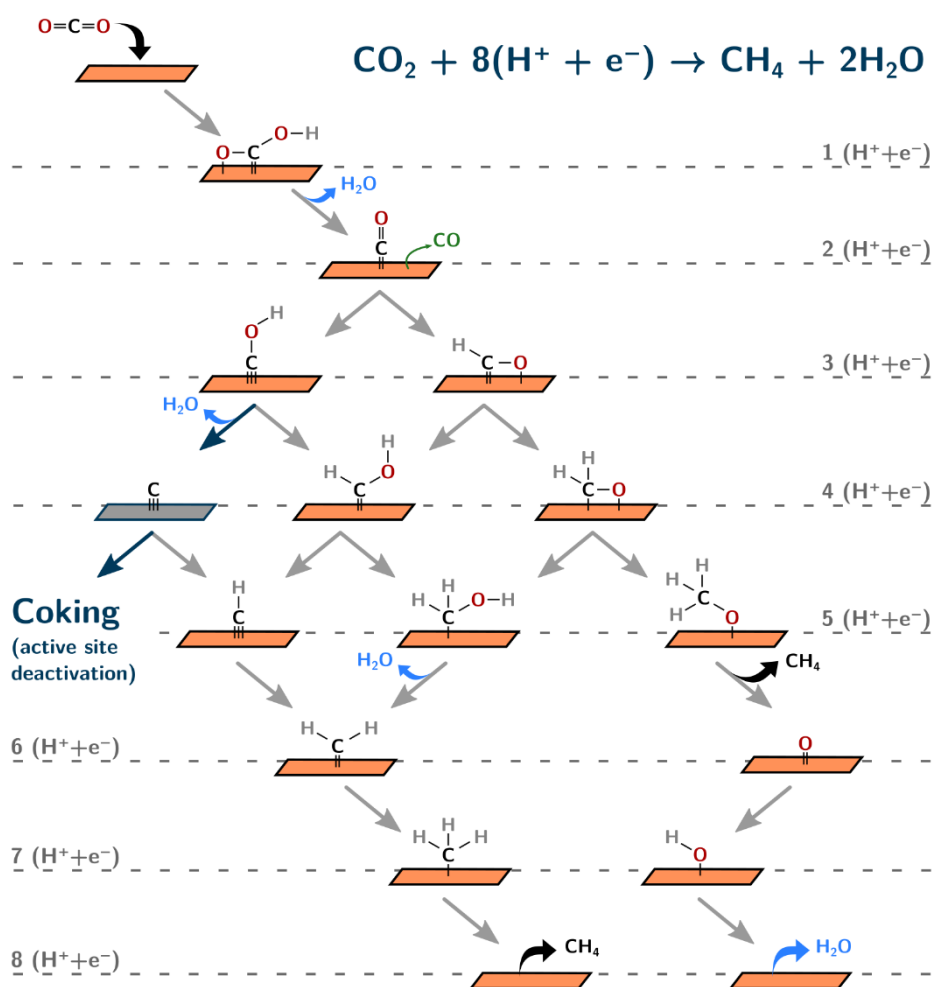
Figure 3. Schematics of the reaction pathways for the CO$_2$RR on Cu electrodes. Each state is separated by a single proton-electron transfer. The bifurcation between the non-coking (right, via *CHO) and coking (left, via *COH, then *C) pathways occurs during *CO hydrogenation.

In Figure 4, we show the adsorption energies of *CO, *CHO, and *COH on Cu(111) and Cu(100) with respect to *CO, protons and electrons at 0 V vs RHE. The transition states to electroreduce *CO to *COH (TS$_{COH}$, black) and *CHO (TS$_{CHO}$, red) are also shown in Figure 4 for the lower-bound case in which the kinetic barriers coincide with the uphill energy differences. However, knowledge of the exact location of the transition states is not required in the following analysis. We will only assume that the thermodynamic differences at 0 V vs RHE of the transition states are in line with those of the final states: $\Delta G_{TS_{CHO}} - \Delta G_{TS_{COH}} \approx \Delta G_{CHO} - \Delta G_{COH}$, and this is justified by the Brønsted-Evans-Polanyi (BEP) relations [56, 58], see section S1.2 in SI for detailed analysis. According to Figure 4, the thermodynamic differences for the formation of *COH and *CHO are 0.16 and 0.21 eV on Cu(100) and Cu(111), respectively. The assumption also seems reasonable considering

13

351 that earlier reports on Cu(111) showed differences of 0.25-0.27 eV in the kinetic barriers of

352 *CHO vs *COH at 0 V vs RHE [36, 59].

353 Based on Equation 3, the potential-dependent difference of Gibbs energies between the

354 transition states of two competing pathways, namely those via *CHO and *COH, is given

355 by Equation 4.

356 $$\Delta G^{\#}_{TS_{CHO}} - \Delta G^{\#}_{TS_{COH}} \approx \Delta G_{TS_{CHO}} - \Delta G_{TS_{COH}} + \left(\beta_{CHO} - \beta_{COH}\right)eU \qquad (4)$$

357 We emphasize that the left-hand side of Equation 4 (i.e. $\Delta G^{\#}_{TS_{CHO}} - \Delta G^{\#}_{TS_{COH}}$) is potential-

358 dependent because the kinetics may change as a function of the applied potential.

359 Conversely, the first difference at the right-hand side (i.e. $\Delta G_{TS_{CHO}} - \Delta G_{TS_{COH}}$) is independent

360 of the applied potential and corresponds to the thermodynamic states at 0 V vs RHE, so that

361 the potential dependence is incorporated by the last term (i.e. $\left(\beta_{CHO} - \beta_{COH}\right)eU$).

362
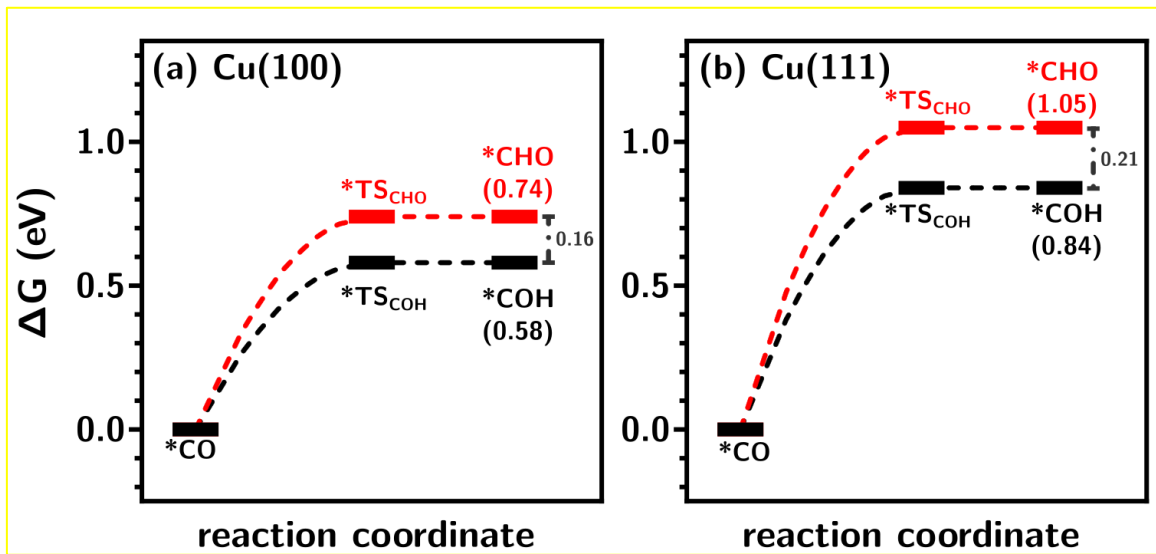
Figure 4. Gibbs energy diagrams for the hydrogenation of *CO on (a) Cu(100) and (b) Cu(111) at 0 V vs RHE.
The formation of *COH (black) and *CHO (red) is shown for both facets. The values in parentheses correspond
to the energies of formation calculated with respect to *CO, protons and electrons. For convenience and without
any impact on the analysis, the transition states are set to the lower-bound case in which they are equal to the
final states (see the text for details). Dashed lines are merely a guide to the eye to connect initial, transition and
final states.

369

370 According to Figure 4, at 0 V vs RHE the *COH-based pathway dominates, but a shift

371 happens when there is a sign change in Equation 4. In other words, the pathways will shift

372 at the potential for which the difference in the energies of the transition state is zero

373 ($\Delta G^{\#}_{TS_{CHO}} - \Delta G^{\#}_{TS_{COH}} = 0$). Given that $\Delta G_{CHO} - \Delta G_{COH} > 0$, in Figure 4, a pathway shift can

374 only happen if $\beta_{CHO} > \beta_{COH}$ and the potential is negative. It is important to emphasize that,

375 based on Equation 4, if the symmetry factors of competing elementary reactions are assumed

376 equal, there is no pathway shift at different applied potentials. However, if $\beta_{CHO} \neq \beta_{COH}$, it

377 is possible to calculate the difference in symmetry factors as:

378 $$\beta_{CHO} - \beta_{COH} \approx \left(\Delta G_{CHO} - \Delta G_{COH}\right)/{-eU} \qquad (5)$$

379   Given that deactivation starts declining on Cu(100) at -1.05 V vs RHE and on Cu(111)

380 at -1.20 V vs RHE in Figure 1, we conclude from Equation 5 that

381 $\left(\beta_{CHO} - \beta_{COH}\right)_{@Cu(100)} \approx 0.15$ and $\left(\beta_{CHO} - \beta_{COH}\right)_{@Cu(111)} \approx 0.18$. We note that Equation 5

382 predicts the difference of the symmetry factors for two competing intermediates. To know

383 one of the individual symmetry factors, it is necessary to know or assume the other one. For

384 instance, assuming $\beta_{COH} = 0.5$, Equation 5 predicts $\beta_{CHO} = 0.65$ for Cu(100) and 0.68 for

385 Cu(111). Alternatively, assuming $\beta_{CHO} = 0.5$, we obtain, using Equation 5, $\beta_{COH} = 0.35$ for

386 Cu(100) and 0.32 for Cu(111).

387   These symmetry factors ($\beta_{COH} = 0.5$ for both facets, $\beta_{CHO} = 0.65$ for Cu(100) and 0.68

388 for Cu(111)) can be used to modify Figure 4 (made at 0 V vs RHE) so as to observe pathway

389 shifts at -1.05 and -1.20 V vs RHE for Cu(100) and Cu(111), respectively. The resulting

390 Gibbs energy diagrams are presented in Figure 5 at the applied potential required to shift the

391 mechanisms from *COH-based (coking pathway) to *CHO-based (non-coking pathway).

392 Altogether, Figures 4 and 5 show that thermodynamics makes the CO_2RR pathway proceed

393 initially via *COH. However, because of the smaller symmetry factors of *COH, kinetics

394 incline the pathway toward *CHO as the potential is increasingly negative.

395   The quality of the predictions made with Equation 5 depends on the accuracy of the

396 calculated adsorption energies in solution, which comprise adsorbate-solvent interactions.

397 While different methods consistently predict low or null solvation stabilization for *CO in

398 H_2O, significant differences (~0.2 eV) are observed for *COH because hydrogen bonding is

399 generally not captured by implicit solvation methods[37, 60, 61]. We evaluated the impact

400 of solvation in Equation 5 (shown in section S1.2) and concluded that it is advisable to

401 account for solvent-adsorbate effects by explicitly including H_2O in the calculations.
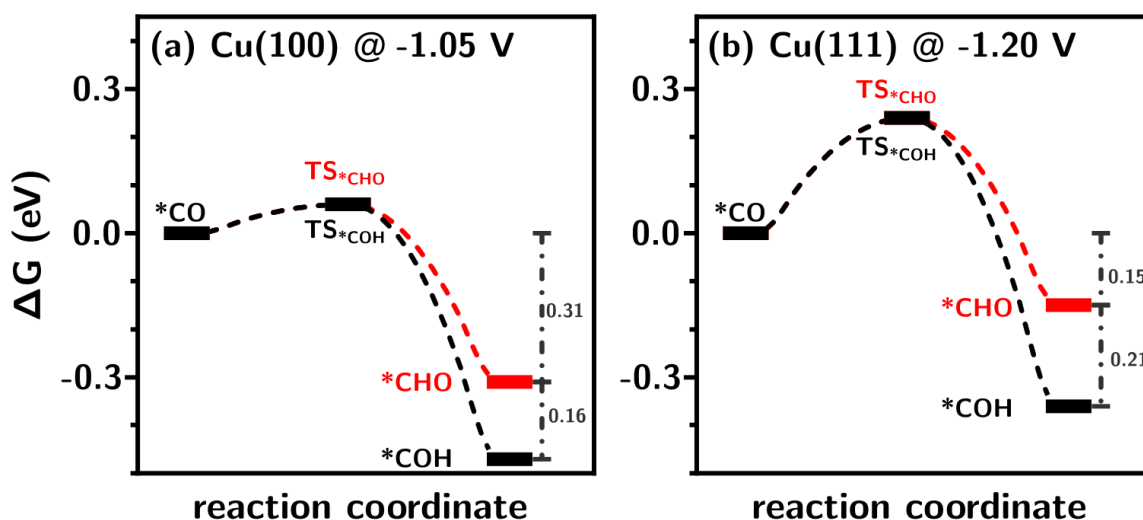
Figure 5. Gibbs energy diagrams for the hydrogenation of *CO to *COH (black) and *CHO (red) at the potentials for which the non-coking pathway becomes kinetically more favorable than the coking pathway. (a) Cu(100) at -1.05 V vs RHE. (b): Cu(111) at -1.20 V vs RHE. The symmetry factors, which affect the kinetic barriers in accordance with Equation 3, are β_{COH} = 0.5 for both Cu(111) and Cu(100), and β_{CHO} = 0.68 for Cu(111) and β_{CHO} = 0.65 for Cu(100), see the text. Note that the differences between *CHO and *COH (0.16 eV on Cu(100) and 0.21 eV on Cu(111)) are potential-independent for a given facet, see also Figure 4. Dashed lines are merely a guide to the eye to connect initial, transition and final states.

Discussion

The interplay between the DFT calculations and experiments provides a new perspective for electrode deactivation due to CH_4 production. Previous studies concluded that *CHO would form favorably at 0 V vs RHE on Cu(100), Cu(111) and Cu(211), and this would lead to the formation of CH_4 after its further hydrogenation [33, 62, 63]. Our calculations have shown otherwise. We found that at low applied overpotentials, *COH is the preferred CO_2RR intermediate up to -1.05 V vs RHE on Cu(100), and up to -1.20 V vs RHE on Cu(111). Further hydrogenation of *COH leads to *C, which can coke and ultimately deactivate the catalysts. The kinetic barriers for *CO hydrogenation to *CHO decrease faster than those of *COH because of the dissimilar symmetry factors, such that there is a potential for which *CHO formation becomes kinetically more favorable. This agrees with our experimental observations, as deactivation for CH_4 production was found for all Cu surfaces at low applied overpotentials (Figure 1).

The coking of the catalyst surface as a result of CH_4 production from CO_2RR is identified as the main reason for catalyst deactivation at low overpotentials. This result sheds

light on why some Cu catalysts seem to deactivate faster than others during CO_2RR. Fast-deactivating catalysts tend to be CH_4-selective [29, 64, 65]. In contrast, both chloride-derived and oxide-derived copper catalysts, which tend to reduce CO_2 and CO to C_2 molecules rather than CH_4, are observed to be stable for several hours, since the formation of C_2 products does not involve *C as an intermediate [9, 15, 16, 65].

We can also use Equation 5 to anticipate the effects of modifying Cu electrodes. In essence, if one seeks to minimize the overpotential without deactivating the electrode, *CHO should be made thermodynamically more stable than *COH and the difference in their symmetry factors brought closer to unity ($\beta_{CHO} - \beta_{COH} \approx 1$). In fact, mild changes in the symmetry factors can lead to a substantial overpotential decrease. For instance, maintaining thermodynamics untouched on Cu(111) (i.e. $\Delta G_{CHO} - \Delta G_{COH} = 0.21 \, \text{eV}$) and modestly increasing the difference in symmetry factors ($\beta_{CHO} - \beta_{COH}$) from 0.18 to 0.25, lower the potential for the pathway shift from -1.2 to nearly -0.8 V vs RHE, according to Equation 5. This would represent a substantial energy saving, as the overpotential would decrease by ~0.4 V. Note in passing that by using a DFT-based microkinetic model, Liu et al. [66] also concluded that stabilization of the transition state for *CO hydrogenation to *CHO enhances the formation rate of CH_4.

A simple means of increasing *CHO's symmetry factor is offered by the BEP relations, which establish a proportionality between the thermodynamics and kinetics of chemical and electrochemical reactions [56, 58]. In this context, stabilizing *CHO thermodynamically will also likely stabilize the transition state from *CO to *CHO, see section S1.2. In doing so, the symmetry factor for the reaction might increase, particularly if the products and the transition state resemble each other, electronically speaking. Since the electronic and geometric structures of metals are usually well correlated [67, 68], a late transition state (one that geometrically resembles the products) might have a symmetry factor close to 1 [58]. In this order of ideas, symmetry factors might be modified by changing surface metal-metal distances via strain and/or alloying.

Before closing the discussion, it is worth mentioning that Nie et al. [35] proposed a simple method to account for the different symmetry factors of electrochemical steps based on the surface dipole moments at the initial and transition states, and the thickness of the double layer. Using that approach, on Cu(111) at -1.20 V vs RHE, it is found that β_{COH} = 0.45, β_{CHO} = 0.51, and the activation energies for *CO hydrogenation to *CHO and *COH

are 0.36 and 0.19 eV. We agree with Nie et al. that the *COH pathway is thermodynamically and kinetically more favorable than that of *CHO at 0 V vs RHE, and that $\beta_{CHO} > \beta_{COH}$. However, their approach predicts the pathway shift to occur at approximately -1.9 V vs RHE, while our experiments show it to occur at -1.2 V vs RHE.

Conclusions

We have provided here electrochemical, XPS and ICP measurements complemented with DFT calculations on the structure- and potential-dependent reduction of CO_2 to CH_4. After ruling out contamination from metal impurities or changes in surface structures as the source of catalytic deactivation, we conclude that CO_2RR to CH_4 on Cu electrodes proceeds via two different, potential-dependent pathways. The first pathway to open, as the applied potential is made more negative than the equilibrium potential, reduces CO_2 to CH_4 via *COH. This pathway may ultimately lead to the coking and deactivation of Cu electrodes. The second pathway proceeds via *CHO and dominates only at potentials more negative than -1 V vs RHE.

DFT calculations show that *COH is more stable than *CHO at 0 V vs RHE. However, a model combining DFT-calculated and experimental data reveals that a pathway shift takes place as the potential is progressively more negative because the facet-dependent symmetry factors for *CHO formation are larger than that for *COH.

Our results also hint toward the important conclusion that the long-term, stable production of CH_4 may be reached if the reaction occurs via the non-coking pathway. On surfaces with Cu(111) or Cu(100) facets, this can be assured by applying suitably large overpotentials. To prevent deactivation and evolve CH_4 at minimal overpotentials, it is advisable to thermodynamically and/or kinetically stabilize *CHO and increase, even modestly, the symmetry factor leading to its formation.

Acknowledgements

References

[1] Y. Hori, A. Murata, R. Takahashi, S. Suzuki, Electrochemical reduction of carbon monoxide to hydrocarbons at various metal electrodes in aqueous solution, Chem Lett, 16 (1987) 1665-1668, https://doi.org/10.1246/cl.1987.1665

[2] Y. Hori, K. Kikuchi, A. Murata, S. Suzuki, Production of methane and ethylene in electrochemical reduction of carbon dioxide at copper electrode in aqueous hydrogencarbonate solution, Chem Lett, 15 (1986) 897-898, https://doi.org/10.1246/cl.1986.897

[3] Y. Hori, A. Murata, R. Takahashi, Formation of hydrocarbons in the electrochemical reduction of carbon dioxide at a copper electrode in aqueous solution, J Chem Soc, Faraday Trans 1, 85 (1989) 2309-2326, https://doi.org/10.1039/F19898502309

[4] K.P. Kuhl, E.R. Cave, D.N. Abram, T.F. Jaramillo, New insights into the electrochemical reduction of carbon dioxide on metallic copper surfaces, Energy Environ Sci, 5 (2012) 7050-7059, https://doi.org/10.1039/C2EE21234J

[5] Z.W. Seh, J. Kibsgaard, C.F. Dickens, I. Chorkendorff, J.K. Nørskov, T.F. Jaramillo, Combining theory and experiment in electrocatalysis: Insights into materials design, Science, 355 (2017) eaad4998, https://doi.org/10.1126/science.aad4998

[6] Z.P. Jovanov, H.A. Hansen, A.S. Varela, P. Malacrida, A.A. Peterson, J.K. Nørskov, I.E.L. Stephens, I. Chorkendorff, Opportunities and challenges in the electrocatalysis of CO_2 and CO reduction using bifunctional surfaces: A theoretical and experimental study of Au–Cd alloys, J Catal, 343 (2016) 215-231, https://doi.org/10.1016/j.jcat.2016.04.008

[7] A. Rendón-Calle, S. Builes, F. Calle-Vallejo, A brief review of the computational modeling of CO_2 electroreduction on Cu electrodes, Curr Opin Electrochem, 9 (2018) 158-165, https://doi.org/10.1016/j.coelec.2018.03.012

[8] S. Nitopi, E. Bertheussen, S.B. Scott, X. Liu, A.K. Engstfeld, S. Horch, B. Seger, I.E.L. Stephens, K. Chan, C. Hahn, J.K. Nørskov, T.F. Jaramillo, I. Chorkendorff, Progress and Perspectives of Electrochemical CO_2 Reduction on Copper in Aqueous Electrolyte, Chem Rev, 119 (2019) 7610-7672, https://doi.org/10.1021/acs.chemrev.8b00705

[9] Y.Y. Birdja, E. Pérez-Gallent, M.C. Figueiredo, A.J. Göttle, F. Calle-Vallejo, M.T.M. Koper, Advances and challenges in understanding the electrocatalytic conversion of carbon dioxide to fuels, Nat Energy, 4 (2019) 732-745, https://doi.org/10.1038/s41560-019-0450-y

[10] D. Bohra, J.H. Chaudhry, T. Burdyny, E.A. Pidko, W.A. Smith, Modeling the electrical double layer to understand the reaction environment in a CO_2 electrocatalytic system, Energy Environ Sci, 12 (2019) 3380-3389, https://doi.org/10.1039/C9EE02485A

[11] Y. Hori, H. Konishi, T. Futamura, A. Murata, O. Koga, H. Sakurai, K. Oguma, "Deactivation of copper electrode" in electrochemical reduction of CO_2, Electrochim Acta, 50 (2005) 5354-5369, https://doi.org/10.1016/j.electacta.2005.03.015

[12] A. Wuttig, Y. Surendranath, Impurity Ion Complexation Enhances Carbon Dioxide Reduction Catalysis, ACS Catal, 5 (2015) 4479-4484, https://doi.org/10.1021/acscatal.5b00808

[13] M.D. Argyle, C.H. Bartholomew, Heterogeneous catalyst deactivation and regeneration: a review, Catalysts, 5 (2015) 145-269, https://doi.org/10.3390/catal5010145

[14] D.W. DeWulf, T. Jin, A.J. Bard, Electrochemical and Surface Studies of Carbon Dioxide Reduction to Methane and Ethylene at Copper Electrodes in Aqueous Solutions, J Electrochem Soc, 136 (1989) 1686, https://doi.org/10.1149/1.2096993

[15] K. Xiang, F. Zhu, Y. Liu, Y. Pan, X. Wang, X. Yan, H. Liu, A strategy to eliminate carbon deposition on a copper electrode in order to enhance its stability in CO_2RR catalysis by introducing crystal defects, Electrochem Commun, 102 (2019) 72-77, https://doi.org/10.1016/j.elecom.2019.04.001

[16] R. Kas, R. Kortlever, H. Yılmaz, M.T.M. Koper, G. Mul, Manipulating the Hydrocarbon Selectivity of Copper Nanoparticles in CO_2 Electroreduction by Process Conditions, ChemElectroChem, 2 (2015) 354-358, https://doi.org/10.1002/celc.201402373

[17] H. Song, M. Im, J.T. Song, J.-A. Lim, B.-S. Kim, Y. Kwon, S. Ryu, J. Oh, Effect of mass transfer and kinetics in ordered Cu-mesostructures for electrochemical CO_2 reduction, Appl Catal B, 232 (2018) 391-396, https://doi.org/10.1016/j.apcatb.2018.03.071

[18] K.J.P. Schouten, E. Pérez Gallent, M.T. Koper, Structure sensitivity of the electrochemical reduction of carbon monoxide on copper single crystals, ACS Catal, 3 (2013) 1292-1295, https://doi.org/10.1021/cs4002404

[19] A. Wuttig, C. Liu, Q. Peng, M. Yaguchi, C.H. Hendon, K. Motobayashi, S. Ye, M. Osawa, Y. Surendranath, Tracking a Common Surface-Bound Intermediate during CO_2-to-Fuels Catalysis, ACS Cent Sci, 2 (2016) 522-528, https://doi.org/10.1021/acscentsci.6b00155

[20] E. Pérez-Gallent, M.C. Figueiredo, F. Calle-Vallejo, M.T.M. Koper, Spectroscopic Observation of a Hydrogenated CO Dimer Intermediate During CO Reduction on Cu(100) Electrodes, Angew Chem Int Ed, 56 (2017) 3621-3624, https://doi.org/10.1002/anie.201700580

[21] E. Bertheussen, A. Verdaguer-Casadevall, D. Ravasio, J.H. Montoya, D.B. Trimarco, C. Roy, S. Meier, J. Wendland, J.K. Nørskov, I.E.L. Stephens, I. Chorkendorff, Acetaldehyde as an Intermediate in the Electroreduction of Carbon Monoxide to Ethanol on Oxide-Derived Copper, Angew Chem Int Ed, 55 (2016) 1450-1454, https://doi.org/10.1002/anie.201508851

[22] I. Ledezma-Yanez, E.P. Gallent, M.T.M. Koper, F. Calle-Vallejo, Structure-sensitive electroreduction of acetaldehyde to ethanol on copper and its mechanistic implications for

568   CO   and   CO$_2$ reduction,   Catal   Today,   262   (2016)   90-94,
569   https://doi.org/10.1016/j.cattod.2015.09.029

570   [23] S. Zhu, B. Jiang, W.-B. Cai, M. Shao, Direct Observation on Reaction Intermediates
571   and the Role of Bicarbonate Anions in CO$_2$ Electrochemical Reduction Reaction on Cu
572   Surfaces, J Am Chem Soc, 139 (2017) 15664-15667, https://doi.org/10.1021/jacs.7b10462

573   [24] E.L. Clark, C. Hahn, T.F. Jaramillo, A.T. Bell, Electrochemical CO$_2$ Reduction over
574   Compressively Strained CuAg Surface Alloys with Enhanced Multi-Carbon Oxygenate
575   Selectivity, J Am Chem Soc, 139 (2017) 15848-15857, https://doi.org/10.1021/jacs.7b08607

576   [25] Y. Hori, O. Koga, H. Yamazaki, T. Matsuo, Infrared spectroscopy of adsorbed CO and
577   intermediate species in electrochemical reduction of CO$_2$ to hydrocarbons on a Cu electrode,
578   Electrochim Acta, 40 (1995) 2617-2622, https://doi.org/10.1016/0013-4686(95)00239-B

579   [26] Y. Terunuma, A. Saitoh, Y. Momose, Relationship between hydrocarbon production in
580   the electrochemical reduction of CO$_2$ and the characteristics of the Cu electrode, J
581   Electroanal Chem, 434 (1997) 69-75, https://doi.org/10.1016/S0022-0728(97)00122-8

582   [27] I. Takahashi, O. Koga, N. Hoshi, Y. Hori, Electrochemical reduction of CO$_2$ at copper
583   single crystal Cu (S)-[n (111)×(111)] and Cu (S)-[n (110)×(100)] electrodes, J Electroanal
584   Chem, 533 (2002) 135-143, https://doi.org/10.1016/S0022-0728(02)01081-1

585   [28] Y. Hori, I. Takahashi, O. Koga, N. Hoshi, Electrochemical reduction of carbon dioxide
586   at various series of copper single crystal electrodes, J Mol Catal A: Chem, 199 (2003) 39-
587   47, https://doi.org/10.1016/S1381-1169(03)00016-5

588   [29] M. Gonçalves, A. Gomes, J. Condeço, R. Fernandes, T. Pardal, C. Sequeira, J. Branco,
589   Selective electrochemical conversion of CO$_2$ to C$_2$ hydrocarbons, Energy Convers Manag,
590   51 (2010) 30-32, https://doi.org/10.1016/j.enconman.2009.08.002

591   [30] J.T. Billy, A.C. Co, Reducing the onset potential of CO$_2$ electroreduction on CuRu
592   bimetallic   particles,   Appl   Catal   B,   237   (2018)   911-918,
593   https://doi.org/10.1016/j.apcatb.2018.06.072

594   [31] J.-F. Xie, J.-J. Chen, Y.-X. Huang, X. Zhang, W.-K. Wang, G.-X. Huang, H.-Q. Yu,
595   Selective electrochemical CO$_2$ reduction on Cu-Pd heterostructure, Appl Catal B, 270 (2020)
596   118864, https://doi.org/10.1016/j.apcatb.2020.118864

597   [32] D. Zang, Q. Li, G. Dai, M. Zeng, Y. Huang, Y. Wei, Interface engineering of Mo$_8$/Cu
598   heterostructures toward highly selective electrochemical reduction of carbon dioxide into
599   acetate, Appl Catal B, 281 (2021) 119426, https://doi.org/10.1016/j.apcatb.2020.119426

600   [33] A.A. Peterson, F. Abild-Pedersen, F. Studt, J. Rossmeisl, J.K. Nørskov, How copper
601   catalyzes the electroreduction of carbon dioxide into hydrocarbon fuels, Energy Environ Sci,
602   3 (2010) 1311-1315, https://doi.org/10.1039/C0EE00071J

603   [34] J. Hussain, H. Jónsson, E. Skúlason, Calculations of Product Selectivity in
604   Electrochemical   CO$_2$ Reduction,   ACS   Catal,   8   (2018)   5240-5249,
605   https://doi.org/10.1021/acscatal.7b03308

606   [35] X. Nie, M.R. Esopi, M.J. Janik, A. Asthagiri, Selectivity of CO$_2$ Reduction on Copper
607   Electrodes: The Role of the Kinetics of Elementary Steps, Angew Chem Int Ed, 52 (2013)
608   2459-2462, https://doi.org/10.1002/anie.201208320

609   [36] C. Shi, K. Chan, J.S. Yoo, J.K. Nørskov, Barriers of Electrochemical CO$_2$ Reduction on
610   Transition   Metals,   Org   Process   Res   Dev,   20   (2016)   1424-1430,
611   https://doi.org/10.1021/acs.oprd.6b00103

[37] A. Rendón-Calle, S. Builes, F. Calle-Vallejo, Substantial improvement of electrocatalytic predictions by systematic assessment of solvent effects on adsorption energies, Appl Catal B, 276 (2020) 119147, https://doi.org/10.1016/j.apcatb.2020.119147

[38] M.T. Tang, H. Peng, P.S. Lamoureux, M. Bajdich, F. Abild-Pedersen, From electricity to fuels: Descriptors for C_1 selectivity in electrochemical CO_2 reduction, Appl Catal B, 279 (2020) 119384, https://doi.org/10.1016/j.apcatb.2020.119384

[39] R. Guidelli, G. Compton Richard, M. Feliu Juan, E. Gileadi, J. Lipkowski, W. Schmickler, S. Trasatti, Defining the transfer coefficient in electrochemistry: An assessment (IUPAC Technical Report), Pure Appl Chem, 86 (2014) 245, https://doi.org/10.1515/pac-2014-5026

[40] J.L. Stickney, I. Villegas, C.B. Ehlers, In situ restoration of atomically well-ordered copper single-crystal electrode surfaces, J Am Chem Soc, 111 (1989) 6473-6474, https://doi.org/10.1021/ja00198a096

[41] Y. Huang, A.D. Handoko, P. Hirunsit, B.S. Yeo, Electrochemical Reduction of CO_2 Using Copper Single-Crystal Surfaces: Effects of CO* Coverage on the Selective Formation of Ethylene, ACS Catal, 7 (2017) 1749-1756, https://doi.org/10.1021/acscatal.6b03147

[42] Q.H. Low, N.W.X. Loo, F. Calle-Vallejo, B.S. Yeo, Enhanced Electroreduction of Carbon Dioxide to Methanol Using Zinc Dendrites Pulse-Deposited on Silver Foam, Angew Chem Int Ed, 58 (2019) 2256-2260, https://doi.org/10.1002/anie.201810991

[43] G. Kresse, J. Furthmüller, Efficient iterative schemes for ab initio total-energy calculations using a plane-wave basis set, Phys Rev B, 54 (1996) 11169, https://doi.org/10.1103/PhysRevB.54.11169

[44] J.P. Perdew, K. Burke, M. Ernzerhof, Generalized Gradient Approximation Made Simple, Phys Rev Lett, 77 (1996) 3865-3868, https://doi.org/10.1103/PhysRevLett.77.3865

[45] G. Kresse, D. Joubert, From ultrasoft pseudopotentials to the projector augmented-wave method, Phys Rev B, 59 (1999) 1758-1775, https://doi.org/10.1103/PhysRevB.59.1758

[46] M. Methfessel, A. Paxton, High-precision sampling for Brillouin-zone integration in metals, Phys Rev B, 40 (1989) 3616-3621, https://doi.org/10.1103/PhysRevB.40.3616

[47] R. Kortlever, J. Shen, K.J.P. Schouten, F. Calle-Vallejo, M.T.M. Koper, Catalysts and Reaction Pathways for the Electrochemical Reduction of Carbon Dioxide, J Phys Chem Lett, 6 (2015) 4073-4082, https://doi.org/10.1021/acs.jpclett.5b01559

[48] Z. Sun, M.M. Sartin, W. Chen, F. He, J. Cai, Y.-X. Chen, Stability of Product Generation during CO Reduction on Copper, J Phys Chem C, 123 (2019) 21467-21477, https://doi.org/10.1021/acs.jpcc.9b03651

[49] Y.-G. Kim, A. Javier, J.H. Baricuatro, D. Torelli, K.D. Cummins, C.F. Tsang, J.C. Hemminger, M.P. Soriaga, Surface reconstruction of pure-Cu single-crystal electrodes under CO-reduction potentials in alkaline solutions: A study by seriatim ECSTM-DEMS, J Electroanal Chem, 780 (2016) 290-295, https://doi.org/10.1016/j.jelechem.2016.09.029

[50] K.J. P. Schouten, E.P. Gallent, M.T.M. Koper, The electrochemical characterization of copper single-crystal electrodes in alkaline media, J Electroanal Chem, 699 (2013) 6-9, https://doi.org/10.1016/j.jelechem.2013.03.018

[51] S. Fletcher, R.G. Barradas, J.D. Porter, The Anodic Oxidation of Copper Amalgam and Polycrystalline Copper Electrodes in LiOH Solution, J Electrochem Soc, 125 (1978) 1960, https://doi.org/10.1149/1.2131336

[52] A. Bagger, R.M. Arán-Ais, J. Halldin Stenlid, E. Campos dos Santos, L. Arnarson, K. Degn Jensen, M. Escudero-Escribano, B. Roldan Cuenya, J. Rossmeisl, Ab Initio Cyclic Voltammetry on Cu(111), Cu(100) and Cu(110) in Acidic, Neutral and Alkaline Solutions, ChemPhysChem, 20 (2019) 3096-3105, https://doi.org/10.1002/cphc.201900509

[53] V.V. Medvedev, M.Y. Popov, B.N. Mavrin, V.N. Denisov, A. Kirichenko, E.V. Tat'yanin, L.A. Ivanov, V.V. Aksenenkov, S.A. Perfilov, R. Lomakin, V.D. Blank, $Cu-C_{60}$ nanocomposite with suppressed recrystallization, Appl Phys A, 105 (2011) 45, https://doi.org/10.1007/s00339-011-6544-4

[54] M. Galaburda, E. Kovalska, B.T. Hogan, A. Baldycheva, A. Nikolenko, G.I. Dovbeshko, O.I. Oranska, V.M. Bogatyrov, Mechanochemical synthesis of carbon-stabilized Cu/C, Co/C and Ni/C nanocomposites with prolonged resistance to oxidation, Sci Rep, 9 (2019) 17435, https://doi.org/10.1038/s41598-019-54007-2

[55] J. Lee, Y. Tak, Electrocatalytic activity of Cu electrode in electroreduction of CO_2, Electrochim Acta, 46 (2001) 3015-3022, https://doi.org/10.1016/S0013-4686(01)00527-8

[56] S. Wang, B. Temel, J. Shen, G. Jones, L.C. Grabow, F. Studt, T. Bligaard, F. Abild-Pedersen, C.H. Christensen, J.K. Nørskov, Universal Brønsted-Evans-Polanyi Relations for C–C, C–O, C–N, N–O, N–N, and O–O Dissociation Reactions, Catal Lett, 141 (2011) 370-373, https://doi.org/10.1007/s10562-010-0477-y

[57] W. Luo, X. Nie, M.J. Janik, A. Asthagiri, Facet Dependence of CO_2 Reduction Paths on Cu Electrodes, ACS Catal, 6 (2016) 219-229, https://doi.org/10.1021/acscatal.5b01967

[58] S.A. Akhade, R.M. Nidzyn, G. Rostamikia, M.J. Janik, Using Brønsted-Evans-Polanyi relations to predict electrode potential-dependent activation energies, Catal Today, 312 (2018) 82-91, https://doi.org/10.1016/j.cattod.2018.03.048

[59] X. Nie, W. Luo, M.J. Janik, A. Asthagiri, Reaction mechanisms of CO_2 electrochemical reduction on Cu(111) determined with density functional theory, J Catal, 312 (2014) 108-122, https://doi.org/10.1016/j.jcat.2014.01.013

[60] Q. Zhang, A. Asthagiri, Solvation effects on DFT predictions of ORR activity on metal surfaces, Catal Today, 323 (2019) 35-43, https://doi.org/10.1016/j.cattod.2018.07.036

[61] F. Calle-Vallejo, R. F. de Morais, F. Illas, D. Loffreda, P. Sautet, Affordable Estimation of Solvation Contributions to the Adsorption Energies of Oxygenates on Metal Nanoparticles, J Phys Chem C, 123 (2019) 5578-5582, https://doi.org/10.1021/acs.jpcc.9b01211

[62] W. Tang, A.A. Peterson, A.S. Varela, Z.P. Jovanov, L. Bech, W.J. Durand, S. Dahl, J.K. Nørskov, I. Chorkendorff, The importance of surface morphology in controlling the selectivity of polycrystalline copper for CO_2 electroreduction, Phys Chem Chem Phys, 14 (2012) 76-81, https://doi.org/10.1039/C1CP22700A

[63] W.J. Durand, A.A. Peterson, F. Studt, F. Abild-Pedersen, J.K. Nørskov, Structure effects on the energetics of the electrochemical reduction of CO_2 by copper surfaces, Surf Sci, 605 (2011) 1354-1359, https://doi.org/10.1016/j.susc.2011.04.028

[64] G. Kyriacou, A. Anagnostopoulos, Electroreduction of CO_2 on differently prepared copper electrodes: The influence of electrode treatment on the current efficiencies, J Electroanal Chem, 322 (1992) 233-246, https://doi.org/10.1016/0022-0728(92)80079-J

698 [65] C.S. Chen, A.D. Handoko, J.H. Wan, L. Ma, D. Ren, B.S. Yeo, Stable and selective
699 electrochemical reduction of carbon dioxide to ethylene on copper mesocrystals, Catal Sci,
700 5 (2015) 161-168, https://doi.org/10.1039/C4CY00906A

701 [66] X. Liu, J. Xiao, H. Peng, X. Hong, K. Chan, J.K. Nørskov, Understanding trends in
702 electrochemical carbon dioxide reduction rates, Nat Commun, 8 (2017) 15438,
703 https://doi.org/10.1038/ncomms15438

704 [67] B. Hammer, J.K. Nørskov, Theoretical surface science and catalysis—calculations and
705 concepts, Adv Catal, 45 (2000) 71-129, https://doi.org/10.1016/S0360-0564(02)45013-4

706 [68] B. Garlyyev, J. Fichtner, O. Piqué, O. Schneider, A.S. Bandarenka, F. Calle-Vallejo,
707 Revealing the nature of active sites in electrocatalysis, Chem Sci, 10 (2019) 8060-8075,
708 https://doi.org/10.1039/C9SC02654A

709